# Effect of Grain Refinement on High Temperature Steam Oxidation of an FeCrAl Alloy

Joshua Rittenhouse<sup>1</sup>, Matthew Luebbe<sup>1</sup>, Andrew Hoffman<sup>2</sup>, Yuzi Liu<sup>3</sup>, Raul B. Rebak<sup>2</sup>, Rinat K. Islamgaliev<sup>4</sup>, Ruslan Z. Valiev<sup>4</sup>, Visharad Jalan<sup>1</sup>, Haiming Wen<sup>1,5,\*</sup>

<sup>1</sup>Department of Materials Science and Engineering, Missouri University of Science and Technology, Rolla, MO 65409, United States

<sup>2</sup>General Electric Research, Schenectady, NY 12309, United States

<sup>3</sup>Center for Nanoscale Materials, Argonne National Laboratory, Lemont, IL 60439, United States
<sup>4</sup>Institute of Physics of Advanced Materials, Ufa University of Science and Technologies, Ufa
450076, Russia

<sup>5</sup>Department of Nuclear Engineering and Radiation Science, Missouri University of Science and Technology Rolla, MO 65409, United States

\*Corresponding author: wenha@mst.edu (H.M. Wen)

# Abstract

FeCrAl alloys are promising candidates to replace Zr alloys as fuel cladding materials in nuclear light-water reactors. Grain refinement has been indicated to improve irradiation resistance. To enhance corrosion resistance as well, the effects of grain refinement on steam corrosion behavior were investigated in this work. Samples of Kanthal D alloy (Fe-21Cr-5Al) with two different grain sizes (coarse-grained and ultrafine-grained) were exposed to steam at 1200 °C for 2 hrs. Results indicate improved steam corrosion resistance in ultrafine-grained Kanthal D with formation of a thinner protective Al oxide layer and the presence of a thin underlying Cr oxide layer.

# 1. Introduction

The environment in a commercial nuclear light-water reactor (LWR) is extreme and poses many severe challenges in terms of material design and implementation [1,2]. More specifically, the fuel cladding that makes up the fuel rods and contains the uranium-bearing fuel pellets must be able to withstand continuous operation at temperatures around 300 °C, exposure to water and steam at such temperature, and extreme radiation exposure, while retaining sufficient mechanical properties so as to prevent rupture and release of fission products [1,3].

Traditionally Zr-based alloys have been used for fuel cladding in both boiling-water reactors (BWRs) and pressurized-water reactors (PWRs) [1]. Zirconium alloys were selected and designed for their resistance to corrosion, resistance to prolonged thermal creep, low neutron absorption, and significant resistance to radiation damage [4–6]. However, under loss-of-coolant accident (LOCA) conditions, which include severely increasing temperatures (>1000 °C), reactions between the Zr cladding and steam occur to produce significant amounts of hydrogen [7]. If not monitored and controlled, release of such hydrogen can result in explosive combustion. Such hydrogen combustion resulted in severe damage to the reactor buildings of units 1, 3, and 4 during the events at the Fukushima Daiichi power plant in March 2011 [8].

Since the events at Fukushima Daiichi, significant investment and efforts have been put forth to develop accident tolerant fuel and cladding (ATF) [9,10]. One avenue of such research has led to the investigation of iron-based FeCrAl alloys. Other than removing the risk of hydrogen production, a significant advantage of such alloys is their ability to form a protective aluminum oxide layer under the high temperature steam conditions encountered in a LOCA [3,9,11]. Alongside such high temperature resistance, such FeCrAl alloys also maintain desirable hydrothermal corrosion resistance under operating conditions through the formation of a more traditional, protective Cr-oxide layer [3].

To further improve the characteristics of FeCrAl alloys and other steel alloys commonly or prospectively used in nuclear applications, grain refinement including nanostructuring has been studied primarily as a means of improving irradiation resistance [12–16]. It has been found that grain boundaries act as sinks for irradiation-induced defects [12–16]. Thus, the premise of such research that has widely been shown is that increasing the fraction of grain boundaries allows for more effective absorption of irradiation-induced defects, enabling retention of a more intact microstructure for longer time under irradiation.

In this work, equal-channel angular pressing (ECAP) is used to produce an ultrafine-grained microstructure (UFG, 100 nm < average grain size < 1 µm). ECAP is a method of severe plastic deformation (SPD) for grain refinement [17–20]. Essentially, ECAP is performed by pressing a material through a die with a sharp (even as sharp as 90°) angle as a means of SPD, which does not change the dimensions of the sample [19]. Multiple passes and changes in orientation of the sample between passes through the die can be utilized to control the degree of deformation and ultimately grain refinement [19].

The oxidation behavior of FeCrAl alloys under many varying experimental conditions has been well studied. I. Roy, et. al. presented a study on the effects of varying Al content on steam oxidation behavior at 400 °C of a Fe-17Cr alloy with significant findings on how oxide layer changes with Al content [21]. A. Chikhalikar, et. al. performed a similar investigation into the influence of adding Al to an Fe-21Cr alloy on the steam oxidation behavior at 400 and 1200 °C and reported differences in oxide formation at the increased temperature [22].

However, the effects of grain refinement on the steam oxidation behavior of FeCrAl alloys remains relatively unstudied. Thus, the work presented herein intends to address such a gap in knowledge. This is accomplished through the examination of the effects of grain

refinement on the oxidation behavior in 1200 °C steam of Kanthal D (KD), a commercially available FeCrAl alloy (nominally Fe-21Cr-5Al). More specifically, KD processed through ECAP to achieve a UFG microstructure followed by exposure to steam at 1200 °C will be compared to an as-received, coarse-grained (CG, average grain size >1μm) counterpart exposed to the same steam environment.

# 2. Methods

# 2.1. Materials and Processing

The composition of KD is given below in Table 1. KD was purchased in the form of cylindrical bar stock with a diameter of 20 mm. This as-received KD will hereafter be referred to as CG KD. Several of the as-received bar stock rods were then used in ECAP processing. Using route B<sub>C</sub>, as detailed in [19], six passes of ECAP at 520 °C were performed. The inside angle between the entrance channel and exit channel of the ECAP die was 120°. The ECAP-processed KD will hence forth be referred to as UFG KD.

Table 1: Composition of KD

	Fe	Cr	Al	Ni	Si	V	Ti	Cu	Mn	С
Wt.%	Bal.	20.57	4.790	0.260	0.240	0.030	0.020	0.020	0.180	0.026

#### 2.2. Steam Oxidation

From the bulk CG KD and UFG KD rods, four 20x2mm disks were cut, two from a CG rod and two from a UFG rod. A 3.5mm hole was drilled towards the edge of each of the disks to allow them to be suspended in the furnace for full exposure to steam. The disks were then sent to General Electric Research for further sample preparation and the steam oxidation experiments as outlined in the following sentences and paragraph. Both sides of each disk were polished using

SiC polishing paper to a 600-grit finish. This polishing was followed by ultrasonic cleaning in purified water and rinsing with methanol.

The disks were suspended in a vertical tube furnace using Pt wire which was used to avoid degradation of the wire itself and for Pt's chemical inertness with regard to the samples themselves. With the samples in place, the furnace was purged through flow of argon. With the system purged, temperature was ramped up at ~10 °C per minute to a target of 1200 °C with argon flowing continuously. At 1200 °C the flow of argon was turned off, and steam generated using purified water was introduced at a flow rate of 5g per minute. Exposure to steam was maintained for two hours. After the two-hour exposure, power to the furnace was shut off, flow of steam was stopped, and argon was reintroduced to bring the environment back to ambient conditions.

# 2.3. Characterization

X-ray diffraction (XRD) was performed using a Philips X'PERT MPD XRD with a Cu source. Patterns were collected between 5° and 90°, and a total scan time of 30 minutes was used. Initial characterization on the micron level was performed using a FEI Quanta 600F scanning electron microscope (SEM). This instrument was equipped with a field emission gun (FEG), a backscatter electron (BSE) detector, and Bruker Xflash 6 energy dispersive x-ray spectroscopy (EDS) detector. Such SEM characterization included identification of oxide spalling sites utilizing elemental (Z) contrast provided by BSE imaging. The samples were Au/Pd sputter coated to improve conductivity and prevent beam drift during SEM observation. ImageJ software was used to measure and quantify the oxide spalling sites from the SEM BSE images.

Following initial SEM surface analysis and quantification of spalling sites, one of the steam corroded CG KD disks and UFG KD disks was cut for initial cross sectional analysis in SEM. The cuts were made using a resin bonded alumina blade in a high-speed precision saw (Allied TechCut 5). The cut pieces were mounted with cross sectional face exposed and were polished with a final step of  $0.02~\mu m$  colloidal silica suspension.

An FEI Scios 2 DualBeam SEM was used for transmission electron microscopy (TEM) sample preparation. This instrument is equipped with a focused Ga ion beam and all necessary attachments to lift out and thin a TEM lamella. Spalling sites were identified using BSE on each of the steam oxidized CG and UFG KD discs as locations for lift-outs. Pt was deposited using the electron beam prior to deposition of a thicker Pt layer using the ion beam to ensure minimal damage to any oxide layers. Lift-outs were mounted to a Cu TEM grid followed by thinning with decreasing current and voltage with final thinning to electron transparency, ~100 nm, performed at 5 kV and 0.3 nA.

For further cross-sectional analysis in terms of thickness measurements of any identified oxide layers, a ThermoFisher Scientific Helios 5 Hydra UX DualBeam plasma focused ion beam (PFIB) SEM was used. A  $\sim$ 150 µm long by  $\sim$ 10 µm wide bead of tungsten was deposited over the surface of each of the steam corroded CG and UFG KD samples. This was followed by bulk milling of a trench  $\sim$ 150 µm long on each of the samples using a 0.15 µA Xe plasma beam with a stage tilt of 52° (ion beam normal to sample surface). Following bulk milling the cross-sectional surface on each sample was cleaned with decreased ion beam currents (down to 4 nA) until the surface was smooth. With the samples tilted at 52°, the electron beam was used to capture cross-sectional images along the lengths of the trench on each of the steam corroded CG and UFG KD samples. From the SEM cross sectional images, a MATLAB script developed by Grant Helmrich

at Oak Ridge National Laboratory was used to trace the identified oxide layer and measure thickness.

An FEI Talos F200X TEM operating at 200 kV was used for scanning TEM (STEM) characterization. This instrument is equipped with an X-FEG field emission gun, a high-angle annular dark field detector (HAADF), and a Super X EDS detector. STEM characterization included identification of the oxide layer and high-resolution EDS maps to detect thinner oxide layers.

Glow discharge optical emission spectroscopy (GD-OES) was performed using a calibrated HORIBA Scientific GD-Profiler 2 instrument equipped with differential interferometry profiling (DiP) for precise depth measurement. A 4 mm circular diameter anode, which determines the area of a measurement, was used with the following source parameters: 700 Pa pressure, power set at 35 W, with pulsing off. Depth profile scans were taken for 3 minutes and monitored live to ensure full measurement of oxide layer(s); level plateau of profile indicated penetration of oxide layer(s) and measurement of bulk material.

Although thorough details on the calibration process of GD-OES is out of the scope of this discussion, it is worth outlining the process in terms of quantitative depth profiling. For quantification, a collection of materials standards with precisely known compositions are required, and these standards should contain significant quantities of elements typically encountered preferably in the form of similar alloys or compounds. Using these standards, GD-OES measurements are made, composition and density of the standards are correlated to those scans, and correlation curves are developed on an elemental basis. Also, with each scan using a standard, depth of the sputtered region is measured using an interferometer or a microscope, and such a measurement over the time sputtered is entered alongside the composition of the standard

allowing for correlation of sputtering rate. In this work, standards for alumina and multiple stainless steels were included in calibration of the machine. In addition, measurements of depth based off the differential interferometry profiling (DiP) system were compared with calculations using calibrated sputtering rates, and the two methods provided proportional results. However, per recommendation from HORIBA Scientific, the calibrated sputtering rate method was used in this work as it is considered to be more accurate in well calibrated systems.

# 3. Results

# 3.1.Oxide Spallation

XRD was performed to gain insight into the crystal structure of oxides on the steam corroded CG and UFG KD. The indexed XRD patterns for the steam corroded CG and UFG KD are shown below in Figure 1. Rhombohedral,  $\alpha$ -Al<sub>2</sub>O<sub>3</sub> was identified which was expected from oxide scale on the surface, and  $\alpha$ -ferrite was also identified which is from the FeCrAl matrix. The presence of the peak corresponding to  $\alpha$ -ferrite at  $\sim$ 82° from the steam corroded UFG KD is believed to result from texture in the UFG KD grain structure.

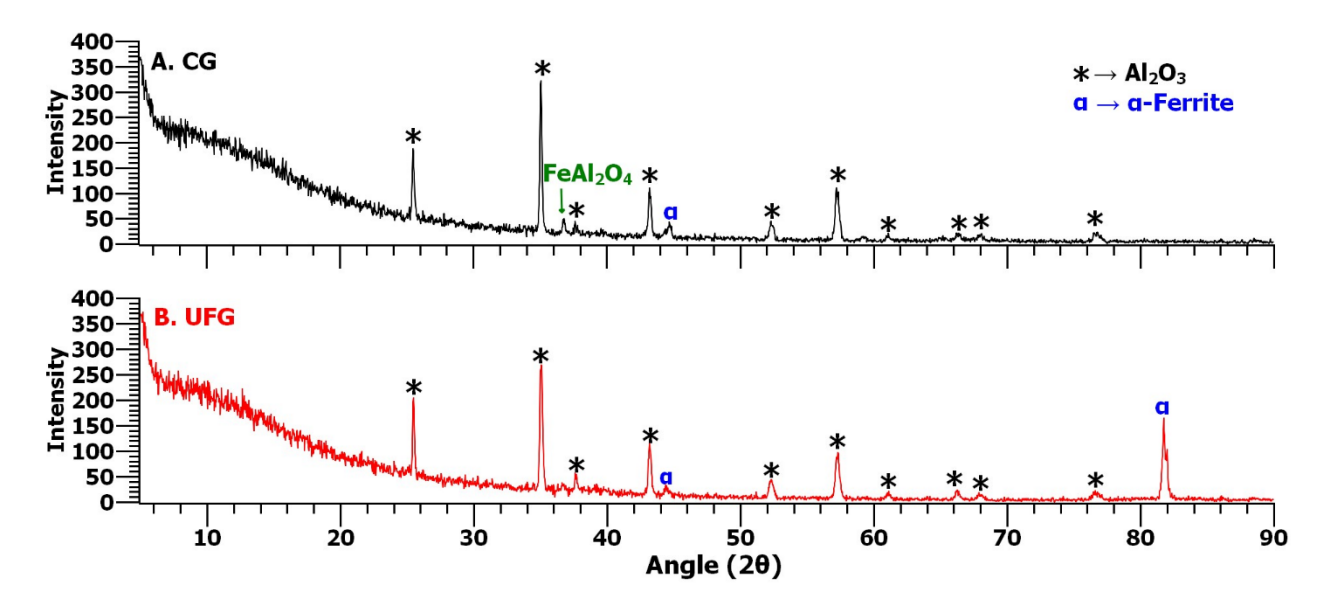


Figure 1: XRD patterns from the steam corroded CG KD (a) and steam corroded UFG KD (b)

In performing initial characterization using SEM, the main objective was to identify any differences on the surface of the oxides of the steam corroded CG and UFG KD. Features with bright elemental contrast under BSE imaging were identified on both the steam corroded CG and UFG KD samples. However, differences were observed between such sites found on the CG KD vs. the UFG KD; the primary difference was size. Examples of such sites are shown in Figure 2. The site shown in Figure 2b is on the larger side of those observed on the surface of the steam corroded UFG KD samples. Many of the sites observed on the UFG KD samples were smaller and more rectangular in nature as opposed to the larger more oval shaped sites observed on the steam corroded CG samples as represented in Figure 2a.

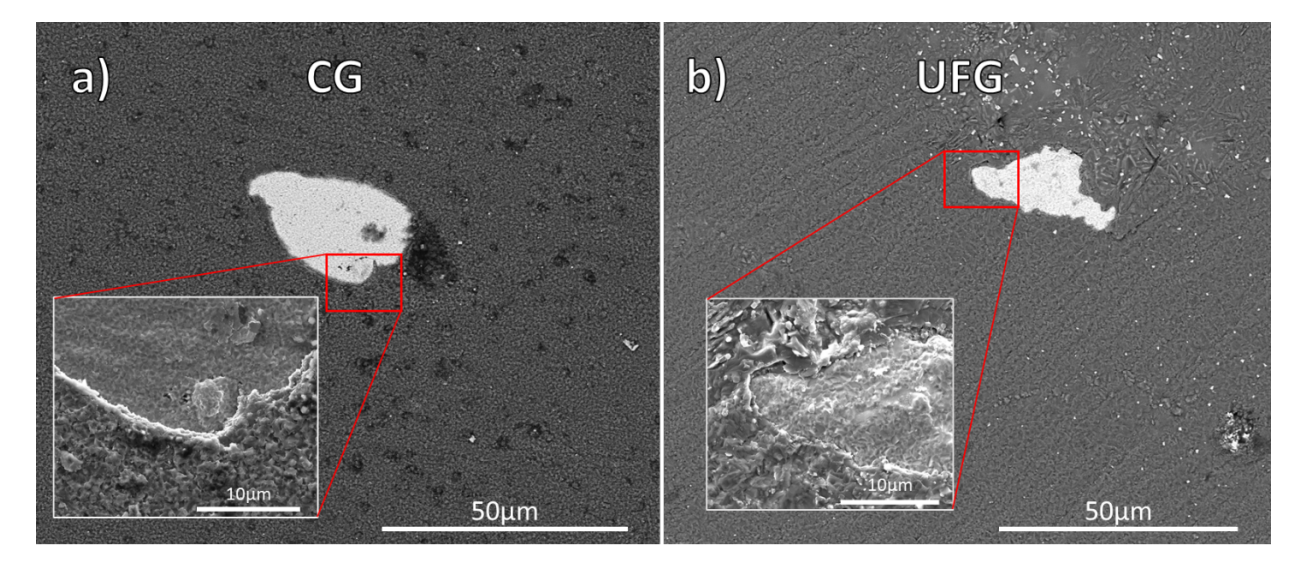


Figure 2: SEM micrographs of representative spalling sites on the surface of the steam corroded CG (a) and UFG (b) samples. Low magnification micrographs were taken using backscatter electron imaging and the inset micrographs are secondary electron images.

To further investigate the exact nature of the assumed spalling sites, SEM EDS compositional mapping was performed. The elemental EDS maps of the site shown in Figure 2a are shown in Figure 3 and are representative of the maps taken of sites observed on both the steam corroded CG and UFG KD. As can be seen from the aluminum elemental map (Figure 3b) and from the oxygen elemental map (Figure 3e), the majority of the surface is covered by an

aluminum oxide layer. However, the sites that appeared with bright elemental contrast under BSE imaging, are devoid of Al and O under EDS mapping and instead show the presence of iron (Figure 3c) and chromium (Figure 3d). This indicates damage or spalling of the aluminum oxide layer, which is likely due to thermal stresses induced during cooling. Also of note, is the observed chromium enrichment in the spalling site. Such enrichment was also observed in the spalling sites on the steam corroded UFG KD samples, and this enrichment is speculated to occur on grain boundaries which will be discussed in more detail in a later section. However, it is not necessarily believed that such chromium enrichment plays a significant role in the observed spallation as such enriched veins are not observed in all the measured sites.

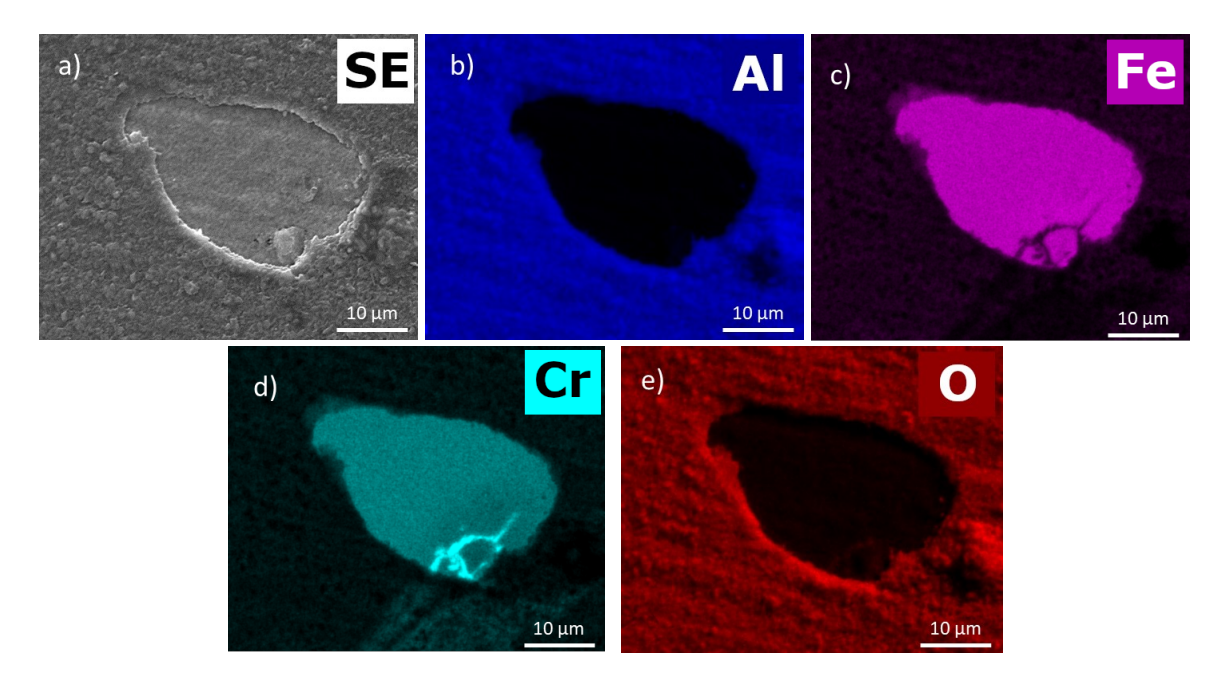


Figure 3: EDS Al (b), Fe (c), Cr (d), and O (e) maps of a representative spalling region as shown in secondary electron image (a) taken from a steam corroded CG KD sample.

To quantitatively determine the differences observed in the spalling sites on the steam corroded CG KD and the UFG KD, area measurements were made utilizing the SEM images and EDS maps similar to those shown in Figure 3. 25 sites were identified and measured from the steam corroded CG KD samples and 27 were identified and measured from the steam corroded

UFG KD samples. With navigation in SEM covering the entire areas of the samples, the sites were randomly identified through such navigation. With the area measurements, area equivalent diameter for the sites along with area fraction and number density were calculated. These quantified values are given in Table 2. As aligns with initial observations, the spalling sites on average are 16.15 μm larger on the steam corroded CG samples compared to the UFG KD samples. However, the density of the spalling sites is 4.11 times greater on the steam corroded UFG KD compared to the steam corroded CG KD.

Table 2: Quantified differences between spalling on steam corroded CG and UFG samples. The error associated with the average diameter values is the standard deviation calculated across the measurements.

Sample	Average Diameter of Spalling Sites (μm)	Area Fraction of Spalling Sites (%)	Number Density of Spalling Sites (m <sup>-2</sup> )
CG	$27.64 \pm 6.44$	3.43	5.42×10 <sup>7</sup>
UFG/ECAP	$11.49 \pm 5.90$	2.92	2.23×10 <sup>8</sup>

# 3.2.Oxide Thickness and Properties

To provide further insight into the characteristics of the oxide(s) formed on the surface of the samples, initial characterization using SEM was performed on the cut cross section samples. SEM BSE images of the oxide layer from such a cross sectional view taken from the steam corroded CG and UFG sample are shown in Figure 4. The oxide layer appears to be fairly uniform on both the steam corroded CG sample and UFG sample. In terms of elemental contrast through BSE imaging, there initially does not appear to be multiple oxide layers of different compositions; however, with the slight nonuniformity on the surface of the oxide on the UFG sample (Figure 4b) and the slight difference in contrast, it was initially believed that a second oxide layer existed on the steam corroded UFG KD sample. Also, as seen in the inset of Figure

4a, there appears to be a vein with an enrichment in chromium. Such enrichment could be similar to that observed in Figure 3 where it is speculated that chromium enrichment could occur along grain boundaries. Likewise, such features were also observed in SEM of the cross sectioned steam corroded UFG KD sample. As can be seen in the inset of Figure 4a, it does not appear that such an enrichment has any localized effects on the uniformity of the alumina layer.

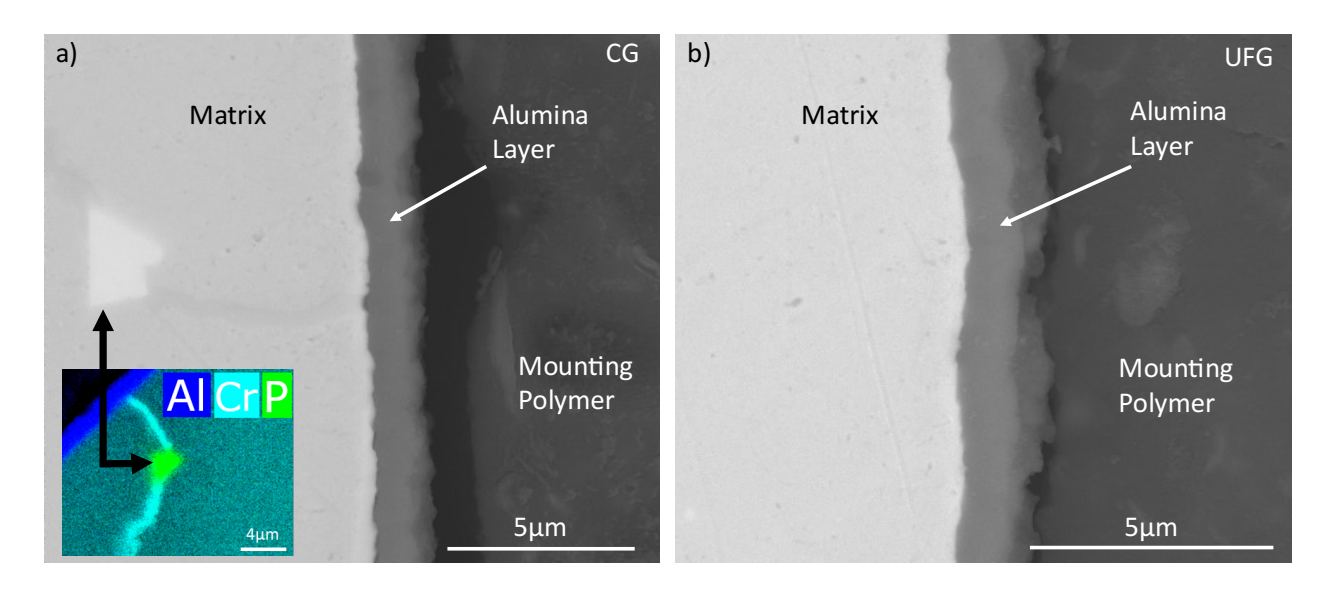


Figure 4: Backscatter electron SEM micrographs of oxide on the surface from a cross sectional view of the steam corroded CG (a) and UFG (b) samples. Inset is a composite EDS map clarifying existence of a P inclusion.

To further investigate the possible existence of any secondary oxide layers on either or both of the steam corroded CG and UFG KD samples, SEM EDS elemental maps were collected. Such EDS maps taken from the steam corroded UFG sample are shown in Figure 5 and are representative of what was observed on both the steam corroded CG and UFG samples. As can be seen in the elemental maps for aluminum, Figure 5b, and oxygen, Figure 5c, the region that appeared to be of slightly different contrast and nonuniformity under BSE imaging on the steam corroded UFG sample (Figure 4b) is still compositionally an aluminum oxide. It is believed that such observations are due to topological effects or rather the sample is oriented such that more of the surface is visible as opposed to a perfect cross-sectional orientation. For further clarification,

it is believed that the mounted sample is oriented such that signal was collected from the surface of the sample behind the plane of the cut which is visible due to the gap between the mounting polymer and the sample. Such orientation is likely to have been caused due to imprecisions in the cutting and mounting process. Similarly, it is believed that the brighter contrast near the aluminum oxide layer, visible in Figure 5a, stems from abrasive cutting as it does not show up as a distinct layer in elemental mapping. Nonetheless, the SEM EDS elemental maps in Figure 5 indicate that a significantly thick aluminum oxide layer is dominant with no secondary layers evident at such a scale.

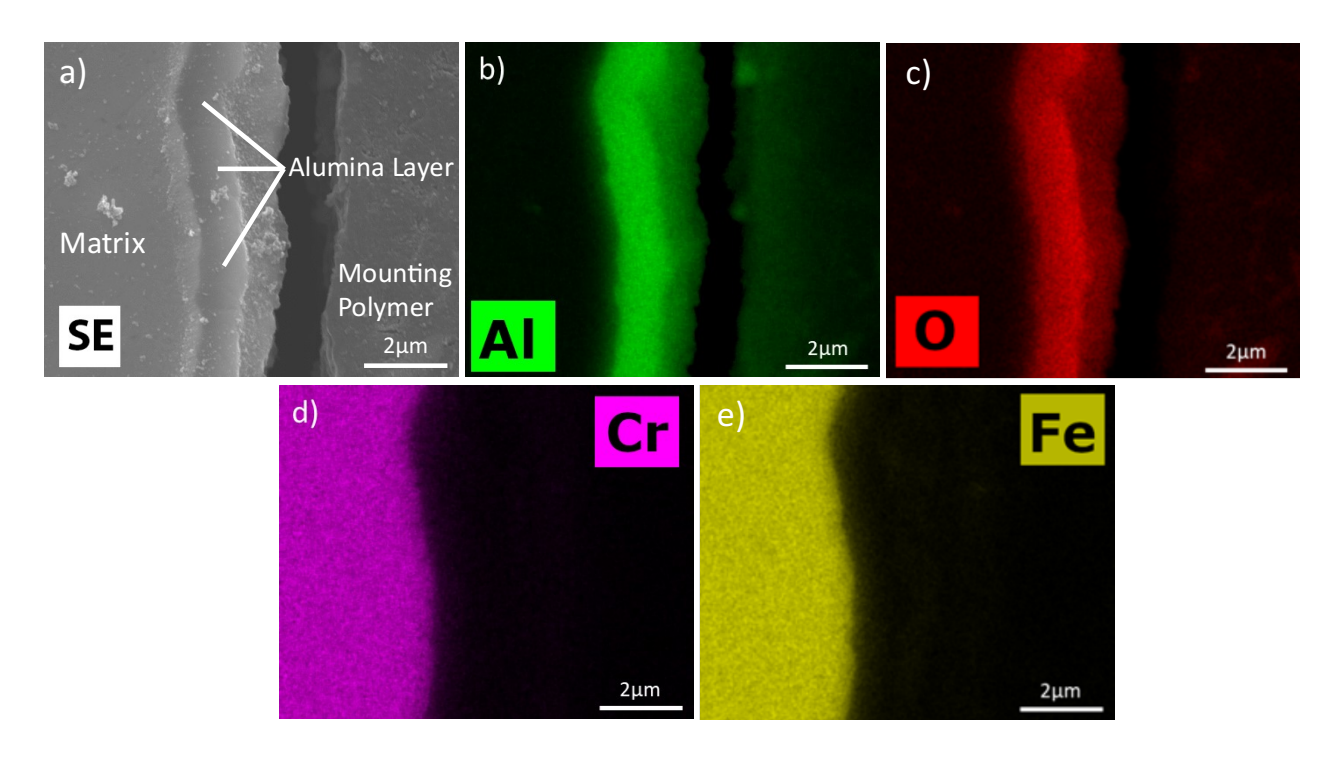
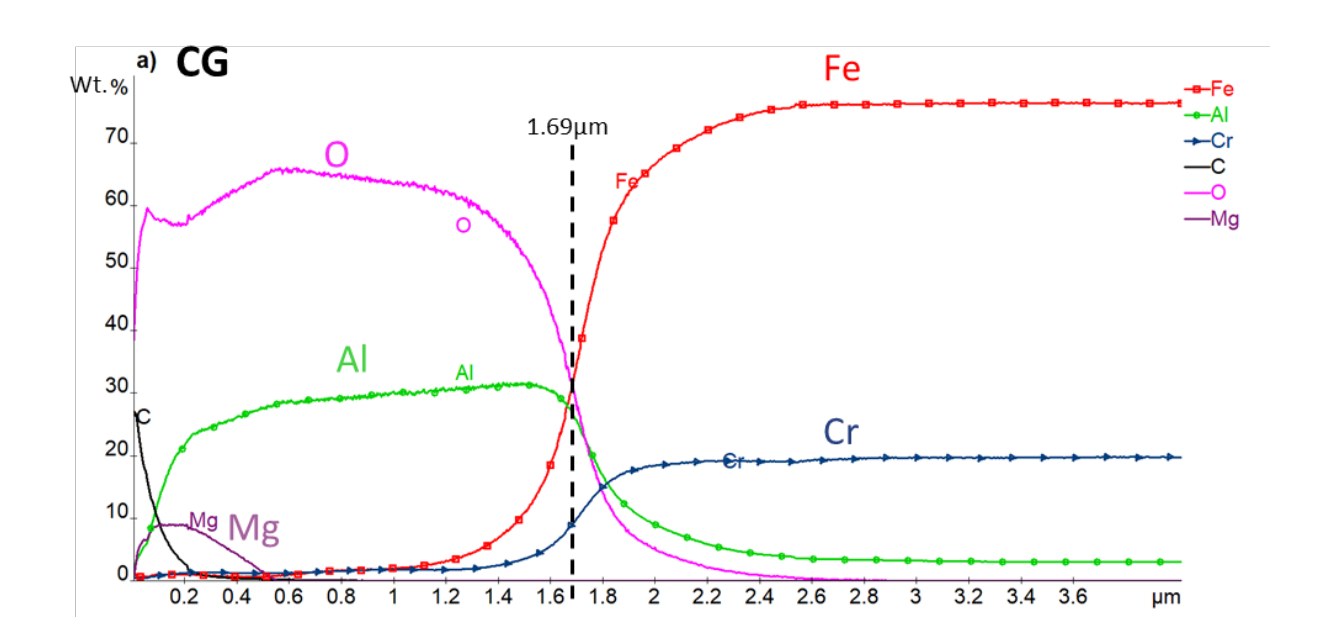


Figure 5: SEM EDS Al (b), O (c), Cr (d), and Fe (e) maps of representative surface oxide structure. Specific region is shown in secondary electron image (a) taken from a steam corroded UFG sample.

Alongside characterization using SEM, Glow discharge optical emission spectroscopy (GD-OES) was performed on the steam corroded CG and UFG KD to gain further insight into the composition and thickness of the oxide layer structures on the samples. GD-OES, when calibrated with relevant material standards both in terms of composition and sputtering rate,

provides compositional vs. depth profiles that are compositionally accurate including light elements down to hydrogen, highly resolving to submicron scale in terms of depth, and statistically relevant in terms of measured area. GD-OES compositional depth profiles taken from the steam corroded CG and UFG KD are shown in Figure 6. With the aforementioned factors in terms of capability, especially the statistically significant area (4 mm diameter circular test region), great weight is put on these results in terms of determining thickness of any oxide layer or layers. As such, it is believed that these measurements in terms of thickness are more accurate than both SEM and TEM analysis especially considering that no destructive sample preparation is required for GD-OES as is the case for the SEM cross sectional analysis, and the thickness measurements are not over a localized area as is the case in TEM.



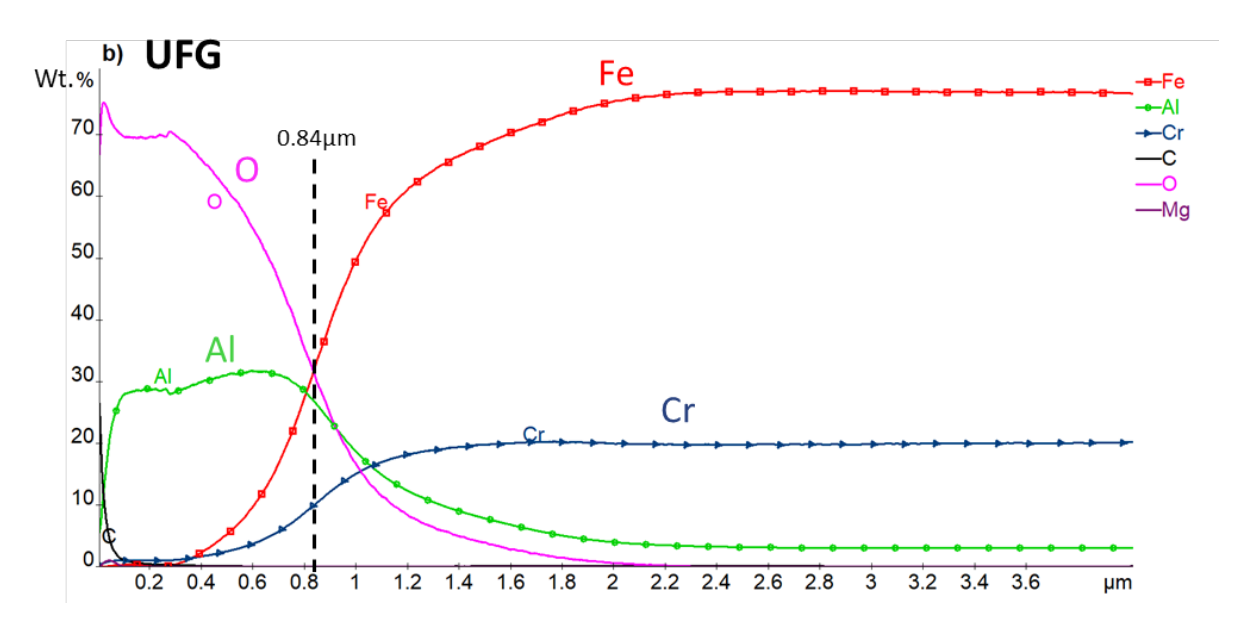


Figure 6: GD-OES composition-depth profiles of surface to bulk region of steam corroded CG (a) and UFG (b) KD samples. Black dashed line represents estimated total oxide thickness.

Utilizing the composition-depth profiles, Figure 6, an immediate difference that is observed between the steam corroded CG and UFG KD samples is the thickness of the aluminum oxide layer. On the steam corroded CG KD the oxide is estimated to be 1.69  $\mu$ m compared to the significantly thinner layer estimated at 0.84  $\mu$ m on the steam corroded UFG KD sample. Another notable difference between the steam corroded CG and UFG KD, is the profile of oxygen concentration through the depth of the oxide. On the steam corroded CG KD, Figure 6a, the O concentration increases in a linear fashion from the surface to ~0.1  $\mu$ m in depth and at ~0.6  $\mu$ m the O profile peaks and then begins a slow decreasing trend; at ~1.2  $\mu$ m in depth a slow transition is made to a steeper linear decrease in O concentration. This steeper decrease occurs from ~1.5  $\mu$ m to ~1.9  $\mu$ m with a difference of 0.4  $\mu$ m. In terms of steam corroded UFG KD, Figure 6b, the O concentration profile shows a quick decrease from an initial peak in concentration where it settles at a plateau at a thickness of ~0.2  $\mu$ m below the surface; at slightly before ~0.4  $\mu$ m below the surface, the profile shifts to a sharply, almost linearly decreasing trend. This almost linear trend begins at ~0.3  $\mu$ m and persists till ~1.1  $\mu$ m for a difference of 0.8

μm which indicates a slower decrease in O concentration with depth compared to the steam corroded CG condition.

Also of note, is the detected presence of magnesium near the surface of the steam corroded CG KD. However, it is believed that the presence of magnesium results from slight impurities in the steam as its concentration peaks more towards the surface and tapers off to indistinguishable levels before even reaching the bulk matrix. That does not explain why magnesium is present in CG sample but not the UFG sample. It could be possible with the indication of enhanced oxygen diffusion through the oxide on the CG sample that there is also enhanced diffusion of magnesium impurities whereas the aluminum oxide on the UFG sample with indicated slower inward oxygen diffusion acts to prevent inward diffusion of such impurities as magnesium. The implications of the aforementioned observations are significant and will be discussed in further detail in the discussion section.

In order to confirm the observed differences in thickness of the aluminum oxide layers on the steam corroded CG and UFG KD, further cross-sectional SEM analysis was performed. More specifically, one  $\sim \! 150~\mu m$  long trench was milled on each of the steam corroded CG and UFG KD samples using a PFIB equipped SEM. Low-magnification SEM images of these trenches are shown in Figure 7c and d from the steam corroded CG and UFG KD respectively. Such milling was performed to obtain cross sectional SEM images while preventing the aforementioned deleterious effects inflicted during mechanical cutting and polishing as well as maintaining a consistent perspective between samples. Higher magnification SEM images used to measure oxide thickness are show in Figure 7a and b for the steam corroded CG KD as well as Figure 7e and f for the steam corroded UFG KD.

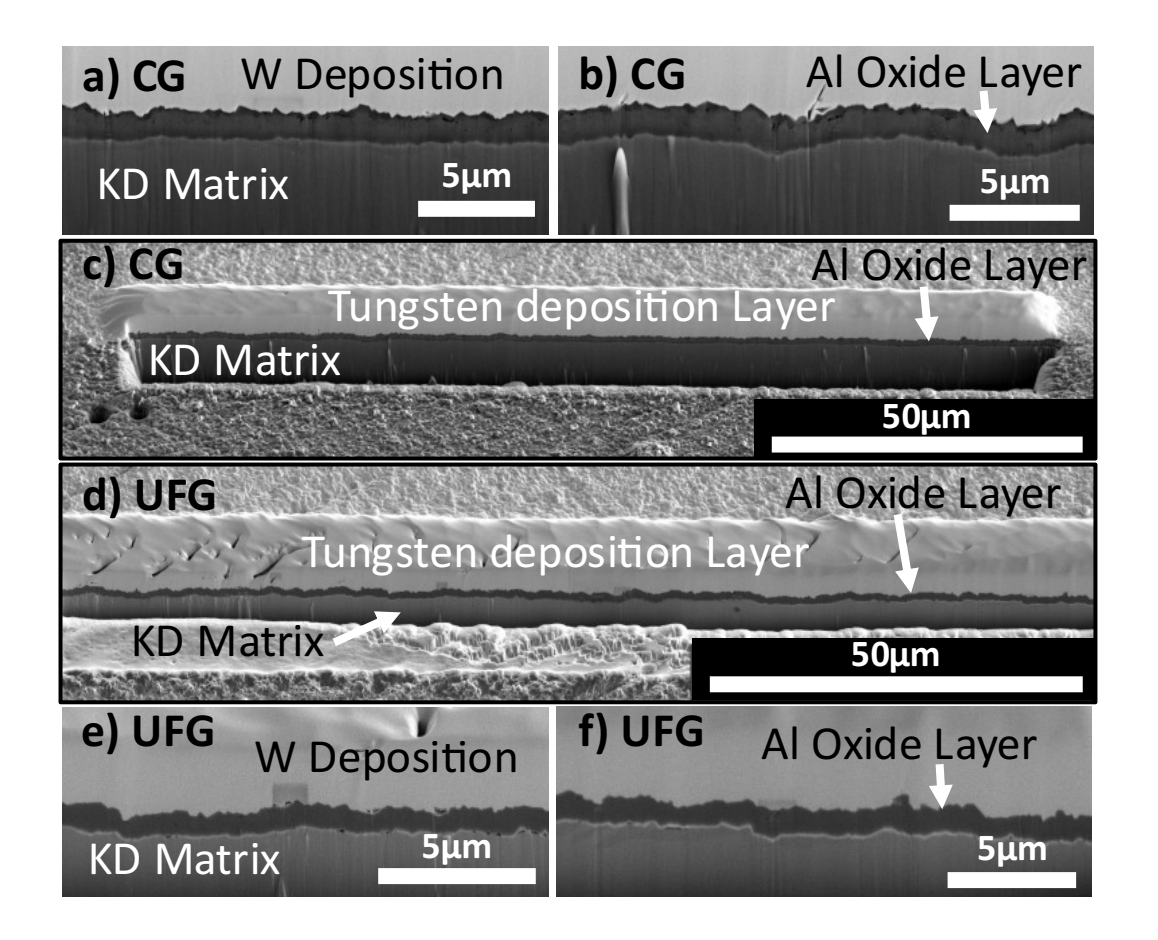


Figure 7: SEM secondary electron images of cross sections from steam corroded CG (a-c) and UFG (d-f) KD prepared using plasma FIB milling. (c) and (d) show low magnification images of ~150 µm long trenches of steam corroded CG and UFG KD, respectively. (a) and (b) show higher magnification images of cross sections from steam corroded CG KD, and (e) and (f) display similarly high magnification images from the steam corroded UFG KD.

Using the higher magnification images like those shown in Figure 7 a, b, e, and f, the aluminum oxide layer was traced within a MATLAB script and thickness was measured. Using the MATLAB script, 10,281 measurements were made from the images of the steam corroded CG KD, and 10,477 measurements were made from the images of the steam corroded UFG KD. With these measurements, the average thickness of the aluminum oxide on the steam corroded CG KD was calculated to be 1.25  $\mu$ m with a standard deviation of 0.13  $\mu$ m; for the steam corroded UFG KD, the average thickness was calculated to be 1.01  $\mu$ m with a standard deviation of 0.13  $\mu$ m. These values reinforce the observation from GD-OES that the aluminum oxide layer

is thicker on the steam corroded CG KD compared to the steam corroded UFG KD. It should be kept in mind when comparing the average thickness values from the SEM analysis to the measured thickness using GD-OES that even though the measurements along the  $\sim \! 150 \, \mu m$  length trenches are significant for FIB/SEM technique, measurements from GD-OES still represent depth profiles over a drastically larger,  $\sim \! 4 \, mm$  diameter area. Therefore, the thickness measurements by GD-OES are considered more statistically accurate.

With the differences in the oxide layer observed between the steam corroded CG and UFG KD in the GD-OES concentration-depth profiles (Figure 6), it was determined that further investigation of the oxide layer and interface was required. Thus, FIB TEM lift-outs were made of the steam corroded CG and UFG KD in order to analyze the oxide and oxide-matrix interface under TEM. The lift-outs were made from regions near spalling sites in order to concurrently gain further insight into such spalling regions alongside intact oxide. Low magnification HAADF STEM images of the oxide, the interface with the bulk matrix, and the spalling region from the steam corroded CG and UFG KD are shown in Figure 8. The thickness of the aluminum oxide on the TEM samples of the steam corroded CG KD and UFG KD was measured to be 1.04±0.09μm and 0.91±0.20μm respectively. This is in reasonable agreement with the observations from the GD-OES results. The measured thickness values from GD-OES are considered more statistically accurate as the areas utilized for measurements in TEM are considerably more localized. Grain structure within the aluminum oxide on both the steam corroded CG and UFG KD can be seen in the HAADF TEM images in Figure 8. The grains that make up the aluminum oxide on the steam corroded UFG KD appear to be more columnar in structure, which is highlighted at higher magnification in Figure 8c, whereas the grain structure of the aluminum oxide on steam corroded CG KD is more equiaxed in nature.

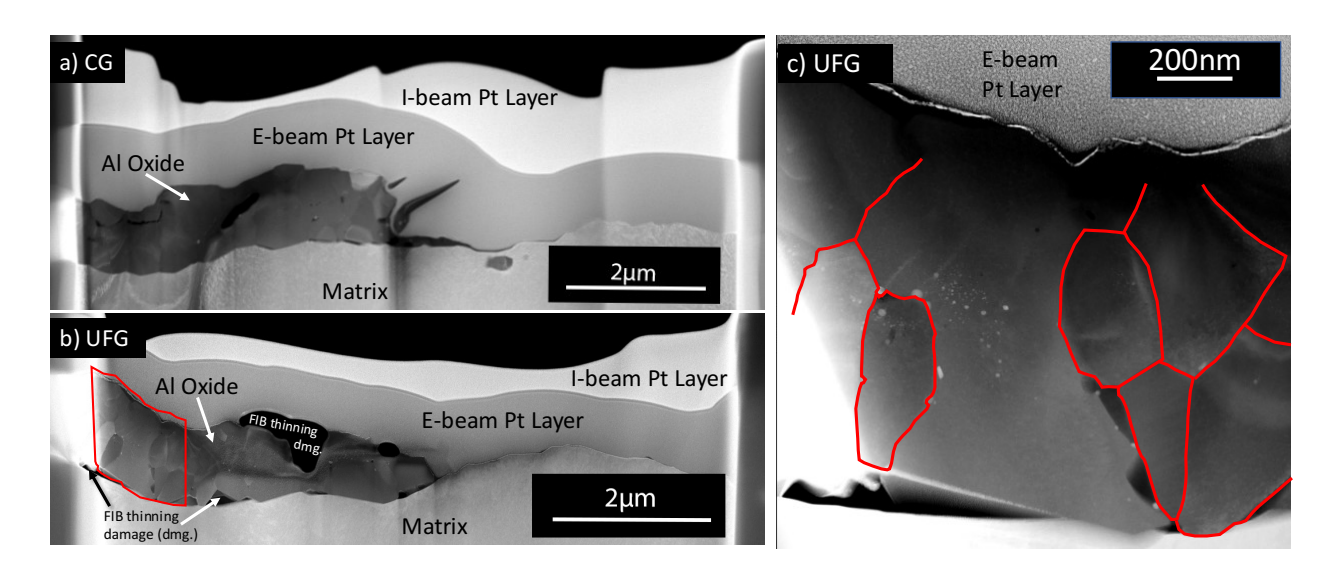


Figure 8: Low magnification STEM HAADF cross sectional images of the alumina structure near a spalled region on the CG sample (a) and UFG sample (b). (c) is a higher magnification STEM HAADF image of the region outlined in red in (b). Red outlines in (c) highlight columnar grain structure seen in the steam corroded UFG KD.

To gain further insight into the oxide layer structure from a compositional perspective and any potential differences that lend explanations to the differences seen in the oxide formation on the steam corroded CG and UFG KD, STEM EDS was performed. Compared to EDS in SEM, EDS in STEM provides much higher resolution. Also, through the use of FIB sample preparation, any damage due to mechanical cutting and polishing present in the cross sectioned samples used for EDS in SEM are not present in the TEM samples. STEM EDS maps of the steam corroded CG KD are shown in Figure 9. As can be observed based on the aluminum (Figure 9c) and oxygen (Figure 9f) maps, the oxide layer is confirmed to be an aluminum oxide as expected. The STEM EDS elemental maps of iron (Figure 9d) and chromium (Figure 9d) further indicate that there are no additional oxide layers on the steam corroded CG KD along with no evidence of an underlying oxide or a shift in oxide formation near a spalling site; this is further reinforced in the elemental map of chromium and oxygen overlayed (Figure 9b) as there is no distinct layer indicating a chromium oxide.

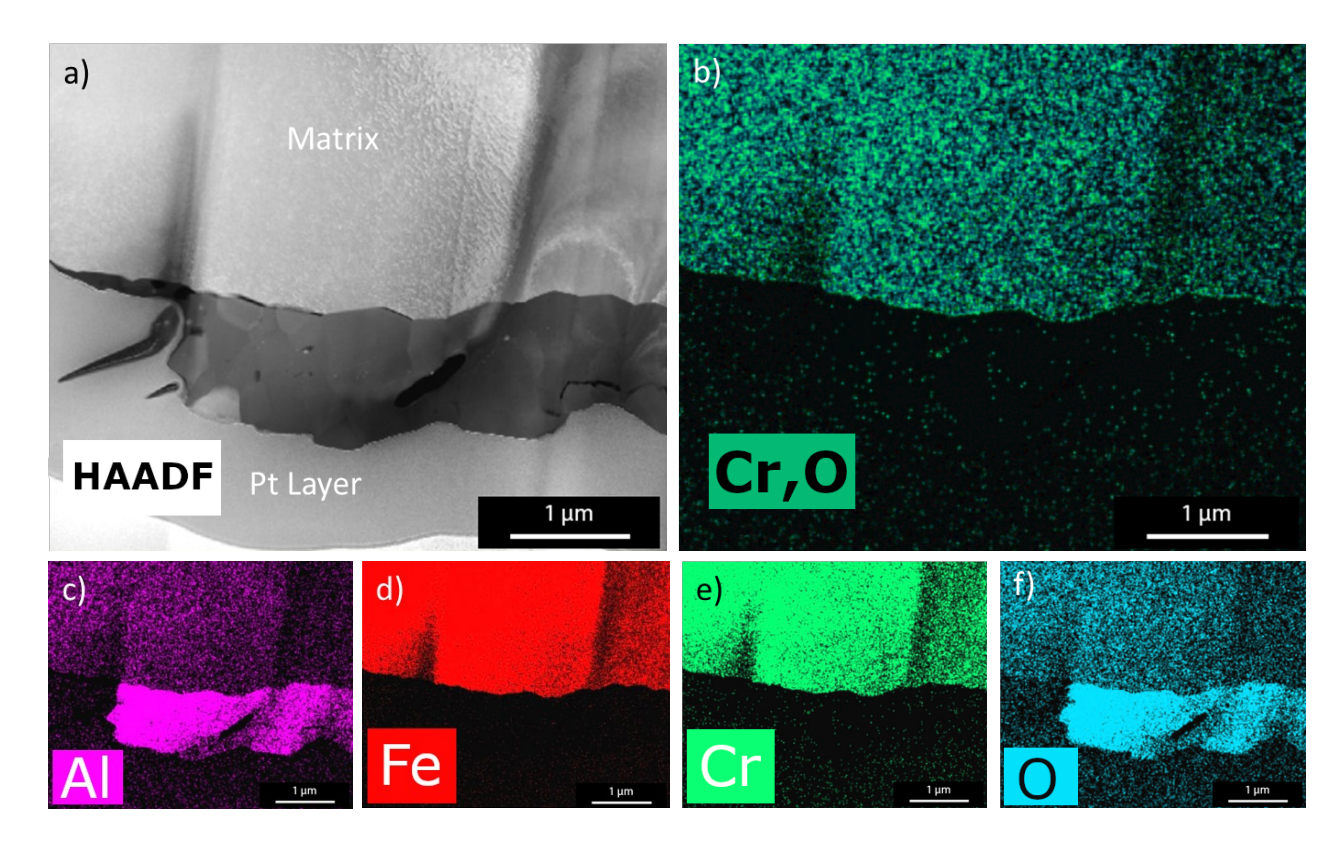


Figure 9: STEM HAADF cross section image of oxide/matrix interface region adjacent to a spalling site (a) and corresponding STEM EDS composite Cr,O (b), Al (c), Fe (d), Cr (e), and O (f) maps taken from a steam corroded CG sample.

STEM EDS elemental maps of the steam corroded UFG KD are shown in Figure 10. The same dominant aluminum oxide layer that is expected is confirmed by elemental maps corresponding to aluminum (Figure 10c) and oxygen (Figure 10f). However, a thin chromium oxide is observed to have formed under the aluminum oxide on the steam corroded UFG KD. This layer can be seen in the overlay map of chromium and oxygen (Figure 10b). This formation of such a chromium oxide layer is a distinct difference as can be observed in the direct comparison between Figure 9b and Figure 10b and of significance in the comparison between the steam corroded CG KD and UFG KD.

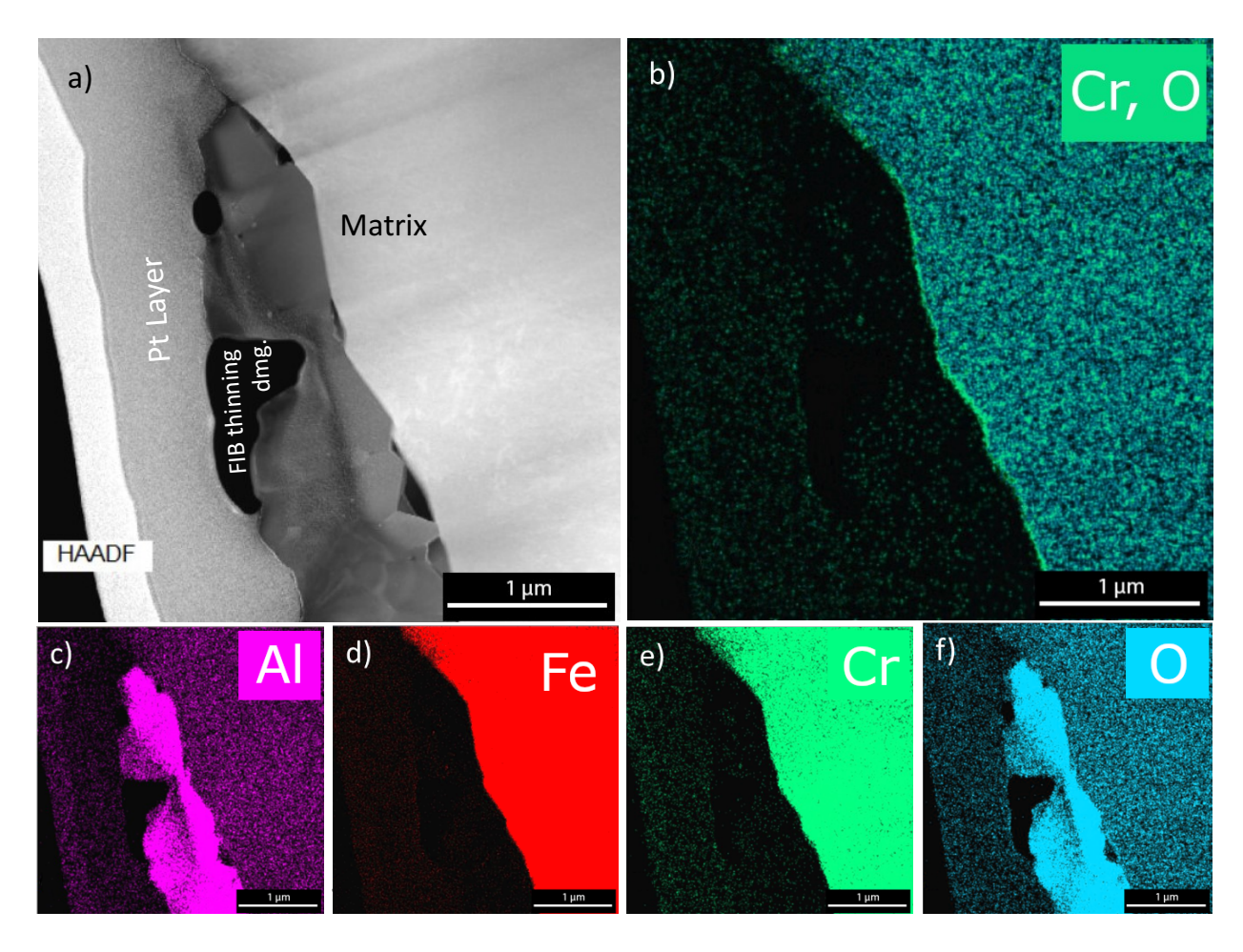


Figure 10: STEM HAADF cross section image of oxide/matrix interface region adjacent to a spalling site (a) and corresponding STEM EDS composite Cr,O (b), Al (c), Fe (d), Cr (e), and O (f) maps taken from a steam corroded UFG sample.

An attempt to collect mass gain/loss data was made. However, it was determined considering the large initial size (20mm in diameter by 2mm thick) and mass (~7 grams) of the samples along with the very small thickness of the oxide scale, that the setup used for the experiments was not sensitive enough to distinguish mass gain stemming from the growth of the oxide from environmental noise within the system/balance. To further illustrate this, calculations were performed considering the oxide as uniform Al<sub>2</sub>O<sub>3</sub> and the thicknesses measured from GD-OES that such oxide growth would only result in about 5.0 and 2.5 milligrams of mass gain for the steam corroded CG and UFG KD, respectively. These values are only 0.07% and 0.04% of the total mass of the samples, so it is logical that a higher degree of sensitivity and stability

within the system would be required for detection of such change. It is left to future work to perform longer steam corrosion experiments or utilize more sensitive thermogravimetric analysis (TGA) equipment with much smaller samples to carefully analyze oxide growth in terms of mass gain.

# 4. Discussion

# 4.1. Oxide Spallation

Spallation of protective oxides is common on a variety of alloys including stainless steels, nickel superalloys, and FeCrAl alloys [23–26]. Thus, the observation of spallation of the aluminum oxide layer on the steam corroded CG and UFG KD was not unexpected. Spallation of a protective oxide is fundamentally due to mismatch in thermal expansion between the oxide and underlying material [27–30]. After formation of the oxide at an elevated temperature, during cooling, as metal typically experiences a higher degree of thermal contraction than the covering oxide, a significant degree of stress builds up in the oxide [26,30,31]. With such applied stress, factors pertaining to the cohesion of the oxide layer dictate the degree and morphology of spallation [30]. As stress is a function of area, thickness of the oxide is also a factor in contributing to spallation [29].

In the case of the steam corroded CG and UFG KD, explanations as to why the spalling sites on the steam corroded UFG KD are smaller and denser compared to the CG KD are needed. As oxide thickness has been established to be a factor in spallation, it is reasonable to assume that the thicker oxide layer observed on the steam corroded CG KD experiences higher degrees of stresses due to mismatch in thermal expansion between oxide and metal. As such, the increased oxide thickness leading to increased stresses is a likely contributor to the increase in spalling site size.

It is also likely that there are differences in cohesion of the aluminum oxide between the steam corroded CG KD and UFG KD. J. Tien, et. al. reported that additions of Y or Sc to various FeCrAl alloys can improve cohesion of the protective oxide to the metal; they argued that such alloying elements act as sinks to vacancies through atom-vacancy complexes and that formation of yttrium or scandium oxide particles prevents growth of voids at the interface between oxide scale and metal matrix [28,32]. A study by J. Kuenzly on oxidation of Ni<sub>3</sub>Al provides further explanation on how a vacancy flux exists due to the Kirkendall effect, which can lead to vacancy supersaturation in the matrix ultimately resulting in void formation [32]. Several other studies also exist on adding reactive elements such as yttrium in FeCrAl alloys to improve cohesion of protective oxides [27,33–35]. It should also be noted that these studies attributed the benefits for addition of alloying elements such as yttrium to reducing lateral oxide growth (growth parallel to the surface) by slowing the inward diffusion of oxygen and outward diffusion of aluminum. The underlying mechanism of lateral growth is the reaction of aluminum and oxygen within the existing oxide layer itself leading to further internal oxide growth. Stress build-up in the oxide layer through such internal growth is reduced as diffusion and subsequent formation is slowed down by yttrium addition [28,33–35].

Yttrium is not present in the CG and UFG KD, however, several of the identified mechanisms leading to the reduction in spalling seen by adding yttrium can be related to findings within the steam corroded UFG KD. Grain boundaries have been found to act as effective defect sinks, which is the premise for utilizing grain refinement as a means of improving irradiation resistance [12–14]. Thus, it follows that in the steam corroded UFG KD, a supersaturation of vacancies leading to potential void formation is prevented by the increased volume fraction of grain boundaries acting as sinks to any source of vacancies, which ultimately contributes to

enhanced oxide cohesion. Also, similar to formation of yttrium oxides to slow or prevent lateral oxide growth presented in the literature, the formation of a thin chromium oxide layer underneath the primary aluminum oxide on the steam corroded UFG KD could act similarly in preventing lateral growth and strain build-up in the primary aluminum oxide layer [28,33–35]. Furthermore, F. A. Golightly, et. al. discussed how a columnar grain structure in the oxide of the yttrium containing FeCrAl likely slows diffusion of oxygen compared to an equiaxed structure in the yttrium free alloy [35]. As a more columnar grain structure is seen in the steam corroded UFG KD compared to more of an equiaxed structure in the steam corroded CG KD, such a factor could further contribute to the differences observed in spallation behavior. Another aspect that could be considered is actual grain size of the oxide as grain size could contribute directly to plasticity. However, the grain size of the oxide on the steam corroded UFG KD is not observed to be significantly different than that on the steam corroded CG KD. Thus, elements within previous discussion are held to have a greater effect in terms of the observed differences in spallation.

#### 4.2. Oxide structure

As observed, there are several differences between the oxide structure formed after exposure to steam on the CG and the UFG KD. Perhaps the most notable difference is that the aluminum oxide formed on the steam corroded UFG KD is thinner than that observed on the steam corroded CG KD. This is likely due, at least in part, to slower oxygen diffusion into and through the aluminum oxide layer on the steam corroded UFG KD as evidenced by the GD-OES compositional depth profiles (Figure 6). As alluded to previously, such slower diffusion of oxygen could be due to the larger columnar grain structure observed in the steam corroded UFG KD [35]. C. Mennicke, et. al. observed a columnar grain structure in the aluminum oxide on a

yttrium containing FeCrAl alloy, and explained that such columnar structure was formed due to a reduction in outward diffusion of aluminum as prevented by yttrium segregation at the metal/oxide interface and along oxide grain boundaries [36]; the reduction in outward diffusion of aluminum would reduce the growth of aluminum oxide grains within the existing oxide resulting in an overall more columnar structure. The formation of yttrium oxides as discussed in aforementioned studies could be present in such a case as well [27,28,32,35]. In the case of the steam corroded UFG KD, rather than yttrium playing a role in preventing outward diffusion of aluminum, the chromium oxide layer observed on the steam corroded UFG KD could reduce the outward diffusion of aluminum as well as further slow the inward diffusion of oxygen.

However, it warrants discussion why chromium oxide is formed on the steam corroded UFG KD but not on the steam corroded CG KD. Not only is Al<sub>2</sub>O<sub>3</sub> more thermodynamically favorable compared to Cr<sub>2</sub>O<sub>3</sub> but Cr<sub>2</sub>O<sub>3</sub> is also known to further oxidize to form volatile gaseous oxides, such as CrO<sub>3</sub>, and oxyhydroxides in steam environments at elevated temperatures above ~800-1000 °C along with chromium itself preferentially forming such gaseous oxides and oxyhydroxides instead of stable Cr<sub>2</sub>O<sub>3</sub> [37–42]. The stability of Al<sub>2</sub>O<sub>3</sub> at high temperatures with positive contributions of chromium especially at lower temperatures is a major consideration and advantage in developing FeCrAl alloys. Nonetheless, the presence of a thin chromium oxide underneath the aluminum oxide is still visible in the steam corroded UFG KD. It has been well established that diffusion along grain boundaries is significantly faster than through grains themselves [43–46]. Thus, the diffusion of aluminum and chromium to the surface of the UFG KD in order to form oxides would be enhanced compared to the CG KD. Such enhanced diffusion of chromium could lead to improved probability of formation of a chromium oxide at the metal-oxide interface where oxygen has diffused through the aluminum oxide layer. Also,

with the formation of chromium oxide underneath the aluminum oxide layer, volatilization of the chromium species would likely be reduced. In review of the literature, formations of significant chromium oxide layers on numerous FeCrAl alloys have been observed alongside aluminum oxides after steam exposure at temperatures ~400 °C [21,22,47]. Wen Qi, et. al. in a study on the addition of molybdenum to a FeCrAl alloy present the observation of a Cr rich nanolayer under a dominant aluminum oxide layer even at steam oxidation conditions of 1200°C, attributing such observations to a degree of chromium oxide vapor becoming saturated in the stable aluminum oxide that formed over top of a previously stable, solid chromium oxide layer [48]. It has also been posed in the literature that during an increase in temperature, an existing chromium oxide layer can facilitate nucleation of an aluminum oxide layer, which tends to grow outwards due to aluminum having a stated higher affinity to react with oxygen [48,49]. Through the addition of such considerations, it seems likely that the observed chromium rich layer underneath the aluminum oxide in this work could potentially be classified as more of a transient oxide that is not completely stable under the experimental conditions [50].

With such observations, it piques interest as to how exactly a multilayered oxide structure transitions into an aluminum oxide dominant structure with an underlying thin chromium oxide layer on the UFG KD with increasing temperature. Further investigation is suggested into the steam corrosion behavior of UFG KD at lower temperatures, representative of LWR normal operating conditions, as well as steam corrosion behavior at elevated temperatures for extended periods.

In relation to the observations of magnesium near the surface of the steam corroded CG KD sample, several studies have been found in the literature on its effects on steam corrosion behavior of FeCrAl alloys [51–53]. However, these studies indicate that the source of

magnesium is present as impurities, on the scale of 80 ppm, in the materials with discussion on how magnesium contributes to the formation of multiple oxide layers including MgAlO phases, and how outward diffusion of magnesium could contribute to a reduction in inward diffusion of oxygen similar to such behavior discussed above [51–53]. Nevertheless, in the case of the steam corroded CG KD, GD-OES results (Figure 6) indicate more of an inward diffusion of magnesium possibly from impurities in the steam, and magnesium containing oxide layers are not observed in either SEM EDS or STEM EDS. It is not necessarily believed that the presence of magnesium in the oxide of the steam corroded CG KD contributes deleteriously to the corrosion behavior of CG KD, but in order to provide any confident statements on such a phenomenon, further investigation is recommended.

# 5. Conclusions

Ultrafine-grained Kanthal D achieved through equal-channel angular pressing, along with coarse-grained Kanthal D, was exposed to steam at 1200 °C for 2 hours. It was observed that an aluminum oxide layer formed and served as a protective layer against corrosion. Spalling of the aluminum oxide layer was observed on both the steam corroded UFG and CG KD. However, spalling sites were smaller but occurred more densely on the steam corroded UFG KD. It was also determined that the aluminum oxide layer is thinner on the steam corroded UFG KD compared to the steam corroded CG KD. This is attributed to slower inward diffusion of oxygen through a more columnar grain structure in the aluminum oxide layer as well as the presence of a thin underlying chromium oxide layer, which is believed to hinder outward diffusion of aluminum on the steam corroded UFG KD. With such findings, it was determined that the resistance of KD to corrosion in a high-temperature steam environment was improved through grain refinement.

# 6. Acknowledgements

This research was financially supported by U.S. Department of Energy, Office of Nuclear Energy (DOE-NE) through the NEET-NSUF (Nuclear Energy Enabling Technology – Nuclear Science User Facility) program (award number DE-NE0008524). J. Rittenhouse acknowledges support from a DOE-NE NEUP UNLP (Nuclear Energy University Program University Nuclear Leadership Program) Graduate Fellowship for its support towards his Ph. D. work. Partial support for H. Wen came from the U.S. National Science Foundation (award number DMR-2207965). Characterization using the Talos F200X was performed at the Center for Nanoscale Materials at Argonne National Laboratory under user proposal 75825. Work performed at the Center for Nanoscale Materials, a U.S. Department of Energy Office of Science User Facility, was supported by the U.S. DOE, Office of Basic Energy Sciences, under Contract No. DE-AC02-06CH11357. The MATLAB script for measuring the oxide thickness in the cross-section SEM and STEM micrographs was developed by Grant Helmrich at Oak Ridge National Laboratory, RZV acknowledges the support in part from Russian Science Foundation (Grant number 22-19-00445). RKI is grateful to the Russian Science Foundation for supporting project 22-23-00714.

# References

- [1] S.J. Zinkle, J.T. Busby, Structural materials for fission & fusion energy, Materials Today. 12 (2009) 12–19. https://doi.org/10.1016/S1369-7021(09)70294-9.
- [2] T. Abram, S. Ion, Generation-IV nuclear power: A review of the state of the science, Energy Policy. 36 (2008) 4323–4330. https://doi.org/10.1016/J.ENPOL.2008.09.059.

- [3] G. Jiang, D. Xu, P. Feng, S. Guo, J. Yang, Y. Li, Corrosion of FeCrAl alloys used as fuel cladding in nuclear reactors, J Alloys Compd. 869 (2021) 159235. https://doi.org/10.1016/J.JALLCOM.2021.159235.
- [4] B. Lustman, Zirconium technology—twenty years of evolution, in: Zirconium in the Nuclear Industry (Fourth Conference), ASTM International, 1979: pp. 5–18.
- [5] H.G. Rickover, L.D. Geiger, B. Lustman, History of the development of zirconium alloys for use in nuclear reactors, U.S. Department of Energy, 1975. https://doi.org/10.2172/4240391.
- [6] A.T. Motta, A. Couet, R.J. Comstock, Corrosion of Zirconium Alloys Used for Nuclear Fuel Cladding, Annu Rev Mater Res. 45 (2015) 311–343. https://doi.org/10.1146/annurev-matsci-070214-020951.
- [7] V.K. Milinchuk, E.R. Klinshpont, V.I. Belozerov, A.V. Zagorodnyaya, Hydrozirconium reaction in heterogeneous compositions, Nuclear Energy and Technology. 3 (2017) 15–18. https://doi.org/10.1016/J.NUCET.2017.03.003.
- [8] M. Hirano, T. Yonomoto, M. Ishigaki, N. Watanabe, Y. Maruyama, Y. Sibamoto, T. Watanabe, K. Moriyama, Insights from review and analysis of the Fukushima Dai-ichi accident, Http://Dx.Doi.Org/10.1080/18811248.2011.636538. 49 (2012) 1–17. https://doi.org/10.1080/18811248.2011.636538.
- [9] B.A. Pint, K.A. Terrani, Y. Yamamoto, L.L. Snead, Material Selection for Accident Tolerant Fuel Cladding, Metallurgical and Materials Transactions E 2015 2:3. 2 (2015) 190–196. https://doi.org/10.1007/S40553-015-0056-7.

- [10] K.A. Terrani, Accident tolerant fuel cladding development: Promise, status, and challenges, Journal of Nuclear Materials. 501 (2018) 13–30.
  https://doi.org/10.1016/J.JNUCMAT.2017.12.043.
- [11] C. Tang, M. Steinbrueck, M. Grosse, A. Jianu, A. Weisenburger, H.J. Seifert, High-Temperature oxidation behavior of kanthal APM and d alloys in steam, in: International Congress on Advances in Nuclear Power Plants, ICAPP 2016, 2016: pp. 2112–2119. https://publikationen.bibliothek.kit.edu/1000063342 (accessed October 2, 2022).
- [12] C. Sun, M. Song, K.Y. Yu, Y. Chen, M. Kirk, M. Li, H. Wang, X. Zhang, In situ Evidence of Defect Cluster Absorption by Grain Boundaries in Kr Ion Irradiated Nanocrystalline Ni, Metallurgical and Materials Transactions A. 44 (2013) 1966–1974. https://doi.org/10.1007/s11661-013-1635-9.
- [13] R. Valiev, Nanostructuring of metals by severe plastic deformation for advanced properties, Nat Mater. 3 (2004) 511–516. https://doi.org/10.1038/nmat1180.
- [14] X. Zhang, K. Hattar, Y. Chen, L. Shao, J. Li, C. Sun, K. Yu, N. Li, M.L. Taheri, H. Wang, J. Wang, M. Nastasi, Radiation damage in nanostructured materials, Prog Mater Sci. 96 (2018) 217–321. https://doi.org/10.1016/J.PMATSCI.2018.03.002.
- [15] J. Duan, H. Wen, L. He, K. Sridharan, A. Hoffman, M. Arivu, X. He, R. Islamgaliev, R. Valiev, Effect of grain size on the irradiation response of grade 91 steel subjected to Fe ion irradiation at 300 °C, J Mater Sci. 57 (2022) 13767–13778.
  https://doi.org/10.1007/s10853-022-07480-6.
- [16] A. Hoffman, M. Arivu, H. Wen, L. He, K. Sridharan, X. Wang, W. Xiong, X. Liu, L. He, Y. Wu, Enhanced Resistance to Irradiation Induced Ferritic Transformation in

- Nanostructured Austenitic Steels, Materialia (Oxf). 13 (2020) 100806. https://doi.org/10.1016/j.mtla.2020.100806.
- [17] V.M. Segal, Severe plastic deformation: simple shear versus pure shear, Materials Science and Engineering: A. 338 (2002) 331–344. https://doi.org/10.1016/S0921-5093(02)00066-7.
- [18] V.M. Segal, Equal channel angular extrusion: from macromechanics to structure formation, Materials Science and Engineering: A. 271 (1999) 322–333. https://doi.org/10.1016/S0921-5093(99)00248-8.
- [19] F. Djavanroodi, M. Ebrahimi, B. Rajabifar, S. Akramizadeh, Fatigue design factors for ECAPed materials, Materials Science and Engineering: A. 528 (2010) 745–750. https://doi.org/10.1016/J.MSEA.2010.09.080.
- [20] R.Z. Valiev, T.G. Langdon, Principles of equal-channel angular pressing as a processing tool for grain refinement, Prog Mater Sci. 51 (2006) 881–981. https://doi.org/10.1016/J.PMATSCI.2006.02.003.
- [21] I. Roy, H. Abouelella, R. Rajendran, A.S. Chikhalikar, M. Larsen, R. Umretiya, A. Hoffman, R. Rebak, Effect of Al concentration on Fe-17Cr alloy during steam oxidation at 400 °C, Corros Sci. 217 (2023) 111135. https://doi.org/10.1016/J.CORSCI.2023.111135.
- [22] A. Chikhalikar, I. Roy, H. Abouelella, R. Umretiya, A. Hoffman, M. Larsen, R.B. Rebak, Effect of aluminum on the FeCr(Al) alloy oxidation resistance in steam environment at low temperature (400 °C) and high temperature (1200 °C), Corros Sci. 209 (2022) 110765. https://doi.org/10.1016/J.CORSCI.2022.110765.

- [23] D. Pan, R. Zhang, H. Wang, C. Lu, Y. Liu, Formation and stability of oxide layer in FeCrAl fuel cladding material under high-temperature steam, J Alloys Compd. 684 (2016) 549–555. https://doi.org/10.1016/J.JALLCOM.2016.05.145.
- [24] R.K.S. Raman, J.B. Gnanamoorthy, S.K. Roy, Synergistic influence of alloy grain size and Si content on the oxidation behavior of 9Cr-1Mo steel, Oxidation of Metals. 42 (1994) 335–355. https://doi.org/10.1007/BF01046754.
- [25] A. Srisrual, K. Pitaksakorn, P. Promdirek, Influence of Water Vapor on Oxide Scale Morphology of Incoloy800HT at 850°C, Applied Mechanics and Materials. 875 (2018) 36–40. https://doi.org/10.4028/WWW.SCIENTIFIC.NET/AMM.875.36.
- [26] Z. Liu, W. Gao, K.L. Dahm, F. Wang, Improved oxide spallation resistance of microcrystalline Ni-Cr-Al coatings, Oxidation of Metals. 50 (1998) 51–69. https://doi.org/https://doi.org/10.1023/A:1018871817578.
- [27] F.H. Stott, G.C. Wood, J. Stringer, The influence of alloying elements on the development and maintenance of protective scales, Oxidation of Metals. 44 (1995) 113–145. https://doi.org/10.1007/BF01046725.
- [28] J.K. Tien, F.S. Pettit, Mechanism of oxide adherence on Fe-25Cr-4Al (Y or Sc) alloys,
   Metallurgical Transactions 1972 3:6. 3 (1972) 1587–1599.
   https://doi.org/10.1007/BF02643050.
- [29] W.J. Quadakkers, D. Naumenko, S. Weinbruch, I. Gurrappa, Factors governing breakaway oxidation of FeCrAl-based alloys Bestimmende Einfluûgro È ûen fu È r die katastrophale Oxidation von FeCrAl-Legierungen, (n.d.).

  https://doi.org/10.1002/(SICI)1521-4176(200004)51:4.

- [30] H.E. Evans, R.C. Lobb, Conditions for the initiation of oxide-scale cracking and spallation, Corros Sci. 24 (1984) 209–222. https://doi.org/10.1016/0010-938X(84)90051-9.
- [31] J.J. Barnes, J.G. Goedjen, D.A. Shores, A Model for stress generation and relief in oxide? Metal systems during a temperature change, Oxidation of Metals. 32 (1989) 449–469. https://doi.org/10.1007/BF00665449.
- [32] J.D. Kuenzly, D.L. Douglass, The oxidation mechanism of Ni3Al containing yttrium,
  Oxidation of Metals. 8 (1974) 139–178. https://doi.org/10.1007/BF00612170/METRICS.
- [33] C. Tang, A. Jianu, M. Steinbrueck, M. Grosse, A. Weisenburger, H.J. Seifert, Influence of composition and heating schedules on compatibility of FeCrAl alloys with high-temperature steam, Journal of Nuclear Materials. 511 (2018) 496–507.
  https://doi.org/10.1016/J.JNUCMAT.2018.09.026.
- [34] F.H. Stott, G.C. Wood, F.A. Golightly, The isothermal oxidation behaviour of FeCrAl and FeCrAlY alloys at 1200°C, Corros Sci. 19 (1979) 869–887. https://doi.org/10.1016/S0010-938X(79)80081-5.
- [35] F.A. Golightly, F.H. Stott, G.C. Wood, The influence of yttrium additions on the oxide-scale adhesion to an iron-chromium-aluminum alloy, Oxidation of Metals. 10 (1976) 163–187. https://doi.org/10.1007/BF00612158.
- [36] C. Mennicke, E. Schumann, M. Rühle, R.J. Hussey, G.I. Sproule, M.J. Graham, The effect of yttrium on the growth process and microstructure of α-Al2O3 on FeCrAl, Oxidation of Metals. 49 (1998) 455–466. https://doi.org/10.1023/a:1018803113093.
- [37] S. Mahboubi, Y. Jiao, W. Cook, W. Zheng, D.A. Guzonas, G.A. Botton, J.R. Kish, Stability of Chromia (Cr2O3)-Based Scales Formed During Corrosion of Austenitic Fe-

- Cr-Ni Alloys in Flowing Oxygenated Supercritical Water, Corrosion. 72 (2016) 1170–1180. https://doi.org/10.5006/1982.
- [38] H. Asteman, J.E. Svensson, L.G. Johansson, M. Norell, Indication of chromium oxide hydroxide evaporation during oxidation of 304L at 873 K in the presence of 10% water vapor, Oxidation of Metals. 52 (1999) 95–111. https://doi.org/10.1023/a:1018875024306.
- [39] S.I. Castañeda, F.J. Pérez, Microstructure and volatile species determination of ferritic/martensitic FB2 steel in contact with Ar + 40 %H2O at high temperatures,
   Oxidation of Metals. 79 (2013) 147–166. https://doi.org/10.1007/s11085-012-9309-3.
- [40] P. Berthod, Kinetics of High Temperature Oxidation and Chromia Volatilization for a Binary Ni–Cr Alloy, Oxidation of Metals. 64 (2005) 235–252. https://doi.org/10.1007/s11085-005-6562-8.
- [41] B.B. Ebbinghaus, Thermodynamics of gas phase chromium species: The chromium oxides, the chromium oxyhydroxides, and volatility calculations in waste incineration processes, Combust Flame. 93 (1993) 119–137. https://doi.org/10.1016/0010-2180(93)90087-J.
- [42] D.R. Gaskell, D.E. Laughlin, Introduction to the Thermodynamics of Materials, 6th ed., CRC Press, Boca Raton, Fl, 2017. https://doi.org/10.1201/9781315119038.
- [43] Y. Mishin, C. Herzig, Grain boundary diffusion: recent progress and future research,

  Materials Science and Engineering: A. 260 (1999) 55–71. https://doi.org/10.1016/S0921-5093(98)00978-2.
- [44] Y. Mishin, C. Herzig, J. Bernardini, W. Gust, Grain boundary diffusion: fundamentals to recent developments, Https://Doi.Org/10.1179/Imr.1997.42.4.155. 42 (2013) 155–178. https://doi.org/10.1179/IMR.1997.42.4.155.

- [45] R.W. Balluffi, Grain boundary diffusion mechanisms in metals, J Electron Mater. 21 (1992) 527–553. https://doi.org/10.1007/BF02669167.
- [46] R. Smoluchowski, Theory of Grain Boundary Diffusion, Physical Review. 87 (1952) 482. https://doi.org/10.1103/PhysRev.87.482.
- [47] H.J. Qu, H. Abouelella, A.S. Chikhalikar, R. Rajendran, I. Roy, J. Priedeman, R. Umretiya, A. Hoffman, J.P. Wharry, R. Rebak, Effect of nickel on the oxidation behavior of FeCrAl alloy in simulated PWR and BWR conditions, Corros Sci. 216 (2023) 111093. https://doi.org/10.1016/J.CORSCI.2023.111093.
- [48] W. Qi, K. Yang, P. Wang, S. Du, C. Bai, X. Wang, Y. Qiao, T. Zheng, L.L. Zhang, X. Zhang, High-temperature steam oxidation behavior of an FeCrAl alloy with controlled addition of Mo, J Mater Sci. 57 (2022) 20909–20927. https://doi.org/10.1007/s10853-022-07920-3.
- [49] D. Naumenko, W.J. Quadakkers, A. Galerie, Y. Wouters, S. Jourdain, Parameters affecting transient oxide formation on FeCrAl based foil and fibre materials, Materials at High Temperatures. 20 (2003) 287–293. https://doi.org/10.1179/mht.2003.034.
- [50] B. Chattopadhyay, G.C. Wood, The transient oxidation of alloys, Oxidation of Metals. 2 (1970) 373–399. https://doi.org/10.1007/BF00604477.
- [51] H. Götlind, F. Liu, J.-E. Svensson, M. Halvarsson, L.-G. Johansson, The Effect of Water Vapor on the Initial Stages of Oxidation of the FeCrAl Alloy Kanthal AF at 900 °C, Oxidation of Metals. 67 (2007) 251–266. https://doi.org/10.1007/s11085-007-9055-0.
- [52] A. Dimyati, H.J. Penkalla, P. Untoro, D. Naumenko, W.J. Quadakkers, J. Mayer, Hightemperature oxidation of FeCrAl alloys: the effect of Mg incorporation into the alumina

- scale, International Journal of Materials Research. 94 (2003) 180–187. https://doi.org/10.3139/IJMR-2003-0037.
- [53] J. Mayer, H.J. Penkalla, A. Dimyati, M. Dani, P. Untoro, D. Naumenko, W.J. Quadakkers, Time dependence of Mg-incorporation in alumina scales on FeCrAl alloys studied by FIBprepared TEM cross sections, Materials at High Temperatures. 20 (2003) 413–419. https://doi.org/10.1179/MHT.2003.048.